RESEARCH ARTICLE

ADVANCED OPTICAL MATERIALS
www.advopticalmat.de

Gigahertz Modulation of a Fully Dielectric Nonlocal Metasurface

Alessandro Pitanti, Gaia Da Prato, Giorgio Biasiol, Alessandro Tredicucci, and Simone Zanotto**

Nonlocal metasurfaces are currently emerging as advanced tools for the manipulation of electromagnetic radiation, going beyond the widely explored Huygens metasurface concept. Nonetheless, the lack of an unified approach for their fast and efficient tunability still represents a serious challenge to overcome. This study reports on the gigahertz modulation of a dielectric slab-based, nonlocal (i.e., angle-dispersive) metasurface, whose operation relies on the optomechanical coupling with a mechanical wave excited piezoelectrically by a transducer integrated on the same chip. Importantly, the metasurface region is free from any conductive material, thus eliminating optical losses, and making the device of potential interest for delicate environments such as high-power apparatuses or quantum optical systems.

1. Introduction

In the last decade, the advent of metasurfaces has brought a revolution in optics, leading to ultracompact lenses, polarization elements, and other special beam manipulation components.[1–4] The great majority of those objects are however developed within a quite particular framework: that of local response. In this approach, each metasurface element (meta-atom) emits radiation that depends only on the incident field exciting that precise meta-atom. While this concept eases the design of metasurfaces—that can be basically constructed as phase, amplitude, or polarization holograms assembling pre-designed unit cells—it possesses intrinsic limitations that can only be overcome by releasing the assumption of local response.[5] In a nonlocal metasurface, the radiation from a meta-atom also depends on the field that excites neighboring elements; equivalently, the response of the metasurface to plane waves is dependent on the angle of incidence.[6] In addition to angular dependence, sharp spectral selectivity, full polarization response, and arbitrary phase manipulation can be enforced, often leveraging on general and powerful symmetry arguments. A representative yet incomplete list of applications includes complex operations such as optical signal processing,[7] image differentiation and edge detection,[8] phase contrast imaging,[9] perfect anomalous reflection,[10] multifunctional wavefront shaping,[11] and space compression.[12,13]

In addition to relieving the limitations of local response, metasurface scientists have been focusing on two other challenging fronts: optical losses mitigation and reconfigurability/modulation. To reduce losses, great efforts have been devoted to the development of dielectric metasurfaces, that are now close to technological maturity.[14–18] Meanwhile, the need for reconfiguration and modulation has been constantly increasing: several mechanisms and materials have been reported to dynamically tune the response of meta-atoms, with speed, energy consumption, ease of fabrication, and electrical control as main figures of merit to be considered.[19–22]

Despite the efforts to advance over all the aforementioned fronts, it appears that to date no study has addressed simultaneously all the three issues of (i) nonlocal response, (ii) absence of optical losses, and (iii) electrically driven high-frequency modulation, greatly limiting the potentials of applying metasurface technologies to high-power optics, quantum photonics and light-based communications. For instance, multi-gigahertz (GHz) metasurface actuation has been observed, without however direct electrical driving.[23,24] Electric control of metasurfaces has already been reported in the last decade[25,26] and is still the subject of recent advances;[27] however, it required conducting

A. Pitanti, G. Da Prato[+], A. Tredicucci
Dipartimento di Fisica "E. Fermi", Università di Pisa
CNR-Istituto Nanoscienze
Largo Pontecorvo 3, Pisa 56127, Italy
E-mail: alessandro.pitanti@unipi.it
A. Pitanti
Paul-Drude-Institut für Festkörperelektronik
Leibniz-Institut im Forschungsverbund Berlin
e. V., 5-7, Hausvogteiplatz, 10117 Berlin, Germany
G. Biasiol
CNR-Istituto Officina dei Materiali
Laboratorio TASC
Trieste 34149, Italy
S. Zanotto
CNR-Istituto Nanoscienze, Laboratorio NEST
Piazza San Silvestro 12, Pisa 56127, Italy
E-mail: simone.zanotto@nano.cnr.it

The ORCID identification number(s) for the author(s) of this article can be found under https://doi.org/10.1002/adom.202401283

[+]Present address: Kavli Institute of Nanoscience, Department of Quantum Nanoscience, Delft University of Technology, Delft 2628CJ, The Netherlands

DOI: 10.1002/adom.202401283

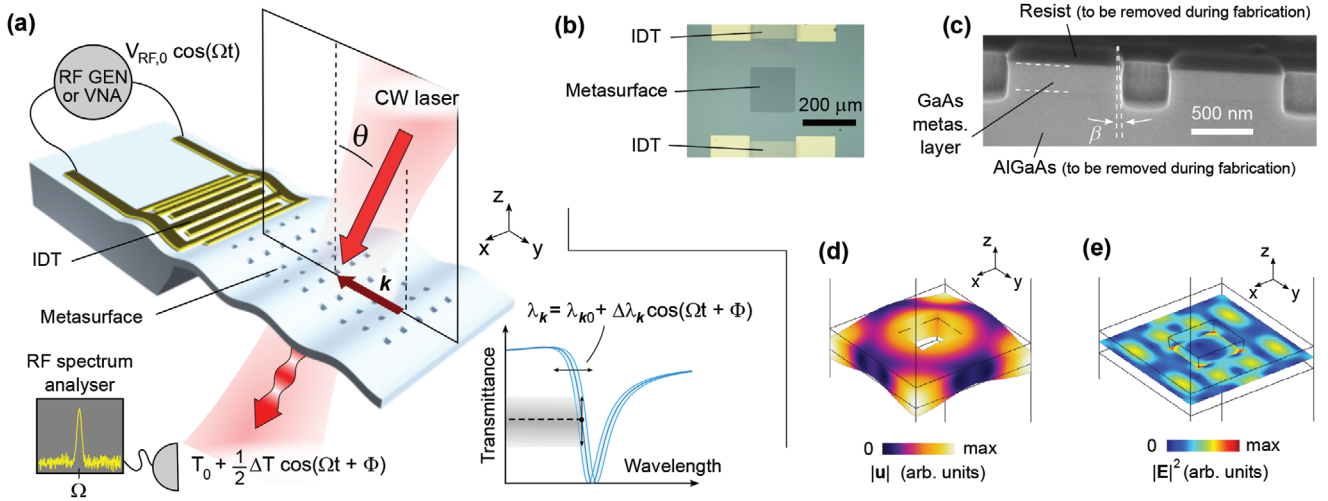

Figure 1. Device concept and resonant modes. a) Rendered scheme of optomechanical modulation in a nonlocal metasurface. A radiofrequency voltage generator (RF GEN) or a vector network analyzer (VNA) is connected to an interdigitated electrode (IDT) monolithically integrated on a piezoelectric chip. Mechanical waves propagate into the metasurface region (consisting of a hole array on a membrane) where coupling with the optical angle-dispersive resonance occurs. The effect is observed as a modulation of transmitted light intensity, mediated by an oscillation of the resonance wavelength. A microscope picture of a portion of the chip is reported in (b). Panel (c) depicts a scanning electron microscope image of a sacrificial chip cross-section collected at an intermediate fabrication step, highlighting the hole sidewall shape. d) and (e) illustrate, respectively, the simulated mechanical displacement field and the optical electric field of the main Bloch eigenmodes involved in the optomechanical coupling process.

elements extending into the optically active metasurface region, inducing optical losses and consequent heating that potentially hinders applications in high-power laser systems. Other reports investigated electrically driven, fully dielectric, and potentially nonlocal metasurfaces; however, the response was there limited to DC or few tens kHz.[28–30]

To overcome those limitations, we have conceived an optomechanical dielectric-slab-based device, where GHz vibrations excited by an interdigitated transducer via the piezoelectric effect propagate towards the photonic-phononic crystal that constitutes the modulating metasurface.[31] Metallic interdigitated transducers (IDTs) are spatially separated from the optically active region, thus completely eliminating optical losses. We developed our device on a monolithic gallium arsenide (GaAs) based platform, extending previous knowledge[32–35] to a membrane-based, free-standing metasurface, which allows for high permittivity contrast and high quality factor (Q) dispersive resonances that can be also interpreted within the photonic crystal framework.[36–38] Moreover, the treatment of photoelastic and moving boundary response of GaAs-based nanoresonators is well established, thus easing the setting of a theoretical background.[39,40] GaAs also compares favorably with other platforms as far as certain metrics are considered. For instance, while aluminum nitride (AlN) has clear advantages regarding integration with silicon,[41,42] AlN cannot host quantum dot and quantum well emitters and detectors, that can be instead realized in GaAs,[43,44] with applications spanning from single photon manipulation[45] to terahertz technology.[46–51] In comparison with lithium niobate ($LiNbO_3$), GaAs has weaker piezoelectric coefficients;[46–52] however, as long as one is interested in creating the metasurface permittivity landscape without introducing other materials and hence by directly etching the piezoelectric material, the use of GaAs involves less demanding processes with respect to $LiNbO_3$.

2. Results

2.1. Sample Design and Operation Principle

Our study relies on the device represented in **Figure 1**a–c, namely, a GaAs/AlGaAs-based monolithic heterostructured chip, where IDTs are placed in close proximity of a substrate-free region where the metasurface is defined.

Fabrication details are given in Section SI (Supporting Information). The metasurface consists of a hole array patterned on a quasi-square lattice in the dielectric membrane (pitches a_x = 1324 nm, a_y = 1317 nm). The metasurface size is 150 × 150 μm^2, large enough to avoid artifacts due to the finite size. The holes have an almost square shape in the $x-y$ plane (x and y sides lengths b_x = 450 nm and b_y = 395 nm, respectively), and a slightly slanted profile in the vertical plane ($\beta = 5°$), as revealed by the cross section of Figure 1c (collected from a sacrificial sample at an intermediate processing step). The main conclusion of this work would be the same if $a_x = a_y$ and $b_x = b_y$, while the non-zero β is instrumental to have a modulation around 1 GHz frequency, as clarified in Section 2.4. The chip is wire-bonded to a printed circuit board (PCB) and mounted on a rotation-translation stage. Thanks to the intrinsic piezoelectricity of GaAs, the IDTs excite a surface acoustic wave (SAW) propagating towards the metasurface membrane; eventually, in the patterned region, the excitation consists of mechanical Bloch modes. In our device, mechanical frequencies in the range 960–1120 MHz can be excited, thanks to IDTs with different pitch (periods from 2.5 to 2.85 μm) facing distinct, but geometrically identical, metasurfaces. Figure 1d represents the simulated profile of the mechanical Bloch mode that plays the most important optomechanical role in our sample. The sample is illuminated with a weakly focused (30 μm) x-polarized laser beam, impinging on the metasurface at an angle θ (further details on the setup in Section SII, Supporting

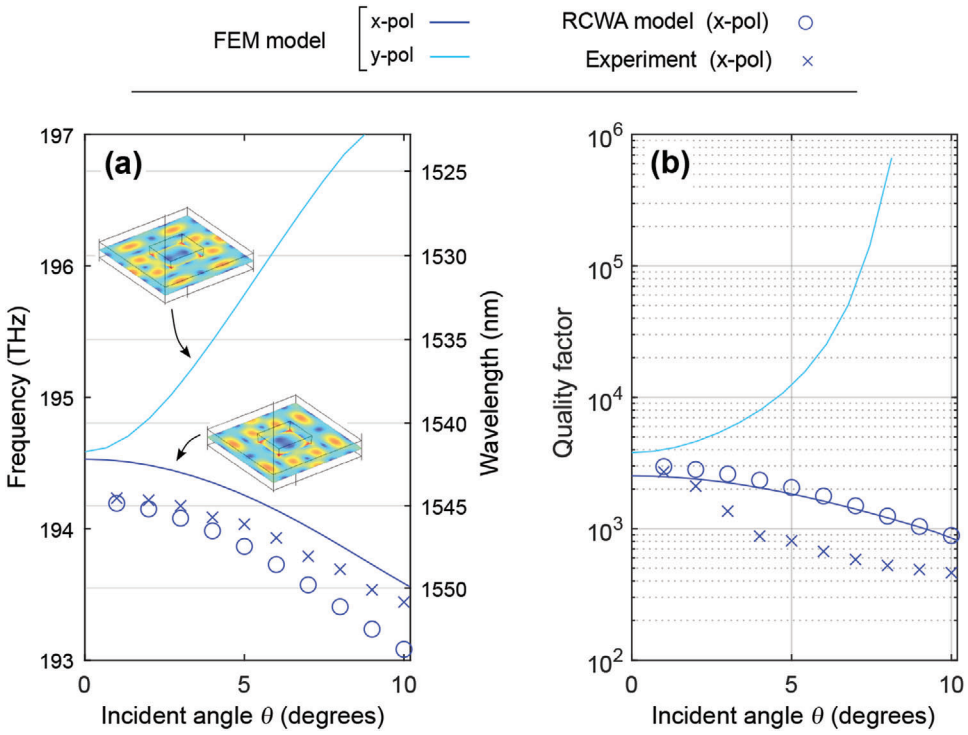

Figure 2. Angular dispersion of photonic modes in the telecommunication wavelength range. Of the two existent modes, we focused our attention on the moderate-Q-factor, red-dispersing mode that couples to x-polarized far-field radiation.

Information). When the beam wavelength-angle pair matches the dispersive resonance condition, a photonic resonance (Figure 1e) is excited. The dispersion of the photonic resonances in the wavelength range of interest is reported in **Figure 2**a,b: the quasi-degenerate doublet occurring at normal incidence gives origin to two branches, where the upper is active under y-polarization, and the lower under x-polarization. The evident angular dependence of the resonances, observable also on the photonic wavevector space (Section SIII, Supporting Information), implies by definition that our system is a nonlocal metasurface. Concerning the quality factors, the upper branch has a diverging Q-factor, witnessing the presence of an accidental BIC at ≈9°; since such a large Q-factor is extremely sensitive to fabrication imperfections, we decided to work with the lower branch, that features a moderately high Q-factor of ≈2700 at normal incidence, then decreasing to 800 in theory (450 in the experiment) for an incident angle $\theta = 10°$. A more detailed analysis of the comparison between experiment and model is reported in Section SIII (Supporting Information). It should be here noticed that the dependence of the Q-factor upon the angle of incidence is not a general feature of nonlocal metasurfaces; different approaches, relying for instance on quasi-guided modes from Brillouin zone folding, can be employed for homogeneous Q-factors.[17]

When the radiofrequency voltage source is on, the IDTs generate a surface acoustic wave, eventually driving the population of mechanical Bloch modes within the metasurface. Such Bloch modes perturb both the hole shape and material refractive index, generating a modulation effect on the photonic resonances, and eventually resulting in a modulation of the laser beam at GHz frequencies (Figure 1a). To develop a quantitative model of the modulation effect, we relied on the quasi-normal mode perturbation theory (QNMPT), elaborating on the concepts and methods illustrated in refs. [53–56]. Quasi-normal modes are eigenstates, corresponding to complex eigenvalues, which emerge from radiative and non-radiative energy losses of open resonators. In our model, another key assumption is an approximation analogous to the Born–Oppenheimer one: since the time scales of near-infrared light waves and that of mechanical vibrations differ by orders of magnitude, we calculated the electromagnetic (e.m.) response assuming that the metasurface shape is "frozen" at a given time within the mechanical cycle. Calculating the e.m. response for all the times of the mechanical cycle leads to the time-dependent (i.e., modulated) e.m. response of the optomechanical metasurface. Moreover, since the shape and refractive index changes induced by the mechanical displacement field are small, one is allowed to adopt a perturbative approach over a suitable basis of electromagnetic Bloch quasi-normal modes. In our case, especially when quasi-normal incidence is considered, the photonic resonance is close to being twofold degenerate, thus calling in principle for a two-mode perturbation theory. However, it can be shown (see Section SV, Supporting Information) that, as long as the photonic and the mechanical Bloch modes are close to the Brillouin zone center, and provided that the mechanical frequency is within the experimental range, the two modes (i.e., polarizations) are not coupled and one can resort to a single-optical-mode perturbation theory. We summarize here the main results of our QNMPT, while the complete derivation can be found in Section SIV (Supporting Information). Indicating with $\boldsymbol{k}$ the photonic Bloch mode wavevector and with $\omega_{\boldsymbol{k},0}$ the dispersive optical resonance frequency for the unperturbed metasurface, it can be

found that the time-dependent complex resonance frequency for the perturbed metasurface is

$$\omega_{\boldsymbol{k}}(t) = \omega_{\boldsymbol{k},0}\,[\,1 + g_{Re}\,\delta_M\,\cos(\Omega t - \Phi_{Re}) + i\,g_{Im}\,\delta_M\,\cos(\Omega t - \Phi_{Im})\,] \tag{1}$$

where Ω is the mechanical frequency, δ_M is the spatio-temporal maximum of the displacement field, $\Phi_{Re(Im)}$ are phase terms defined in Section SIV (Supporting Information), and the couplings $g_{Re(Im)}$ are given by the following formulas:

$$g_{Re} = f_K\,g_{Re}^{(0)} = \frac{f_K}{\omega_{\boldsymbol{k},0}}\sqrt{\Re(\omega_{\boldsymbol{k},0}\Delta_{Re})^2 + \Re(\omega_{\boldsymbol{k},0}\Delta_{Im})^2} \tag{2}$$

$$g_{Im} = f_K\,g_{Im}^{(0)} = \frac{f_K}{\omega_{\boldsymbol{k},0}}\sqrt{\Im(\omega_{\boldsymbol{k},0}\Delta_{Re})^2 + \Im(\omega_{\boldsymbol{k},0}\Delta_{Im})^2} \tag{3}$$

Here, f_K is a real, adimensional quantity that describes the effectiveness of the coupling between the mechanical mode of Bloch wavevector $\boldsymbol{K}$ and the electromagnetic field. In principle, for an infinitely extended metasurface, $f_K = \delta(\boldsymbol{K})$, i.e., f_K is a Dirac delta centered at the origin (the Γ point) of the Brillouin zone, meaning that only those phonons can induce optomechanical modulation. However, we have postulated an "effectively coupled region" scheme (see Section SIV.A, Supporting Information) such that, in the real space, QNMPT integrals are limited to a finite portion of the metasurface with size of the order of σ^{eff}. The factor f_K is then given by

$$f_K = \sum_{m,l}\alpha_{m,l}\cos(a_x\,K_x\,m + a_y\,K_y\,l) \tag{4}$$

where

$$\alpha_{m,l} = \frac{\exp\left\{-\left[\left(\frac{a_x m}{\sigma^{\text{eff}}}\right)^2 + \left(\frac{a_y l}{\sigma^{\text{eff}}}\right)^2\right]\right\}}{\sum_{m',l'}\exp\left\{-\left[\left(\frac{a_x m'}{\sigma^{\text{eff}}}\right)^2 + \left(\frac{a_y l'}{\sigma^{\text{eff}}}\right)^2\right]\right\}} \tag{5}$$

Equations (4) and (5) enable the coupling with mechanical modes at $\boldsymbol{K} \neq 0$, and will be later instrumental to interpret the experimental data (see Section 2.3). In Equations (2–3), the quantities Δ_{Re} and Δ_{Im}, both being in general complex, directly originate from the perturbative integrals calculated over the single unit cell for the moving boundary (MB) and photoelastic (PE) effects: $\Delta_{Re} = \Delta_{\text{MB},\,Re} + \Delta_{\text{PE},\,Re}$ and $\Delta_{Im} = \Delta_{\text{MB},\,Im} + \Delta_{\text{PE},\,Im}$. We report here the expression for the $\Delta_{\text{MB},\,Re}$ term:

$$\Delta_{\text{MB},Re} = -\frac{1}{2D_{\text{uc}}\delta_{\text{ref}}}\int_{\partial D_{\text{uc}}} \mathrm{d}S\,\Re\left[\boldsymbol{n}\cdot\boldsymbol{u}_{\boldsymbol{K},N}^{P}\right]\left(\Delta\varepsilon\,\boldsymbol{E}_{\parallel,-\boldsymbol{k}}^{P}\cdot\boldsymbol{E}_{\parallel,\boldsymbol{k}}^{P} - \Delta\eta\,\boldsymbol{D}_{\perp,-\boldsymbol{k}}^{P}\cdot\boldsymbol{D}_{\perp,\boldsymbol{k}}^{P}\right) \tag{6}$$

The integral is performed over the boundary surface that delimits the dielectric material unit cell (region ∂D_{uc}) and the surrounding air. $\boldsymbol{n}$ is the outgoing unit vector normal to the boundary; $\Delta\varepsilon = \varepsilon_{\text{GaAs}} - 1$ and $\Delta\eta = 1/\varepsilon_{\text{GaAs}} - 1$. $\boldsymbol{u}_{\boldsymbol{K},N}^{P}$ is the periodic part of the mechanical Bloch wavefunction of Bloch wavevector $\boldsymbol{K}$ and mode index N. $\boldsymbol{E}_{\parallel,\boldsymbol{k}}^{P}$ is the periodic part of the $\boldsymbol{k}$-Bloch-wavevector electric field eigenfunction, projected parallelly to the boundary surface. Analogously, $\boldsymbol{D}_{\perp,\boldsymbol{k}}^{P}$ is the displacement field projected perpendicularly to the boundary surface. Notice that the $\boldsymbol{E}$ and $\boldsymbol{D}$ fields come in pairs with $\boldsymbol{k}$ and $-\boldsymbol{k}$, without complex conjugation: this is a key feature of QNMPT, where the ordinary orthogonality relations of Bloch functions no longer holds. Rather, one has to rely on right and left eigenvectors of the Maxwell equation operator, that, in the case of periodic systems, consist of the $(\boldsymbol{k}, -\boldsymbol{k})$ pair. Finally, D_{uc} is a normalization integral that in general assumes complex values, and δ_{ref} is a reference displacement (originating from the mechanical field numerical solver). The term $\Delta_{\text{MB},\,Im}$ is given by Equation (6) with $\Re[\boldsymbol{n}\cdot\boldsymbol{u}_{\boldsymbol{K},N}^{P}]$ replaced by $\Im[\boldsymbol{n}\cdot\boldsymbol{u}_{\boldsymbol{K},N}^{P}]$. The real and imaginary PE terms have a similar formulation, whose explicit expressions have been reported in the Section SIV.A (Supporting Information). It should be noticed that, in our system, moving boundary and photoelastic terms are of the same order of magnitude.

The presence of complex quantities in Equation (1) implies that both the real and imaginary part of $\omega_{\boldsymbol{k}}$ are modulated in time, i.e., that both resonance frequency and quality factor of the dispersive resonance can be tuned optomechanically. Noticeably, since in principle $\Phi_{Re} \neq \Phi_{Im}$, the trajectory of $\omega_{\boldsymbol{k}}(t)$ in the complex plane is an elliptical curve. Moreover, in the terminology of quantum optomechanics, our system exhibits in principle both dispersive and dissipative coupling. It will however turn out from the numerical calculations that $g_{Im}/g_{Re} \approx 10^{-2}$, thus the dissipative contribution is negligible, at least within the approximations mentioned so far.

We will now derive how the modulation of the resonance frequency can be detected by means of a spectroscopic modulation experiment. The key theoretical assumption is that the metasurface transmittance follows a Fano line shape, as predicted by single-mode coupled-mode theory:[57]

$$T(\omega) = \left|\tau + \frac{\Im(\omega_{\boldsymbol{k}})\,(\rho + i\tau)}{\omega - \Re(\omega_{\boldsymbol{k}}) - i\Im(\omega_{\boldsymbol{k}})}\right|^2 \tag{7}$$

Here, ρ and τ are the off-resonance reflection and transmission coefficients (fulfilling $\rho^2 + \tau^2 = 1$), which are reasonably unaffected by the mechanical motion. The temporal modulation of T stems from the dependence of $\omega_{\boldsymbol{k}}$ upon the mechanical action. Employing Equation (1), the approximation $g_{Im} \ll g_{Re}$, and making the wavelength explicit, the following expression is obtained:

$$T(\lambda, t) = T_0(\lambda) + \frac{1}{2}\Delta T(\lambda)\cos\left(\Omega t - \Phi_{Re} + \pi\right) \tag{8}$$

where the static term $T_0(\lambda)$ is obtained from Equation (7) by replacing $\omega_{\boldsymbol{k}}$ with the static frequency $\omega_{\boldsymbol{k},0}$. The modulation term amplitude is given by

$$\Delta T(\lambda) = 2\left.\frac{\mathrm{d}T_0}{\mathrm{d}\lambda}\right|_{\lambda_{\boldsymbol{k},0}}\lambda_{\boldsymbol{k},0}\,g_{Re}\,\delta_M \tag{9}$$

where $\lambda_{\boldsymbol{k},0} = 2\pi c/\omega_{\boldsymbol{k},0}$. Equations (8) and (9) are the main link between theory and experiment: the RF component of the transmitted light at Ω is in fact proportional to $|\Delta T|$. In our experiment, where we analyzed the transmitted light using a high frequency detector coupled with a spectrum analyzer, we were unable to

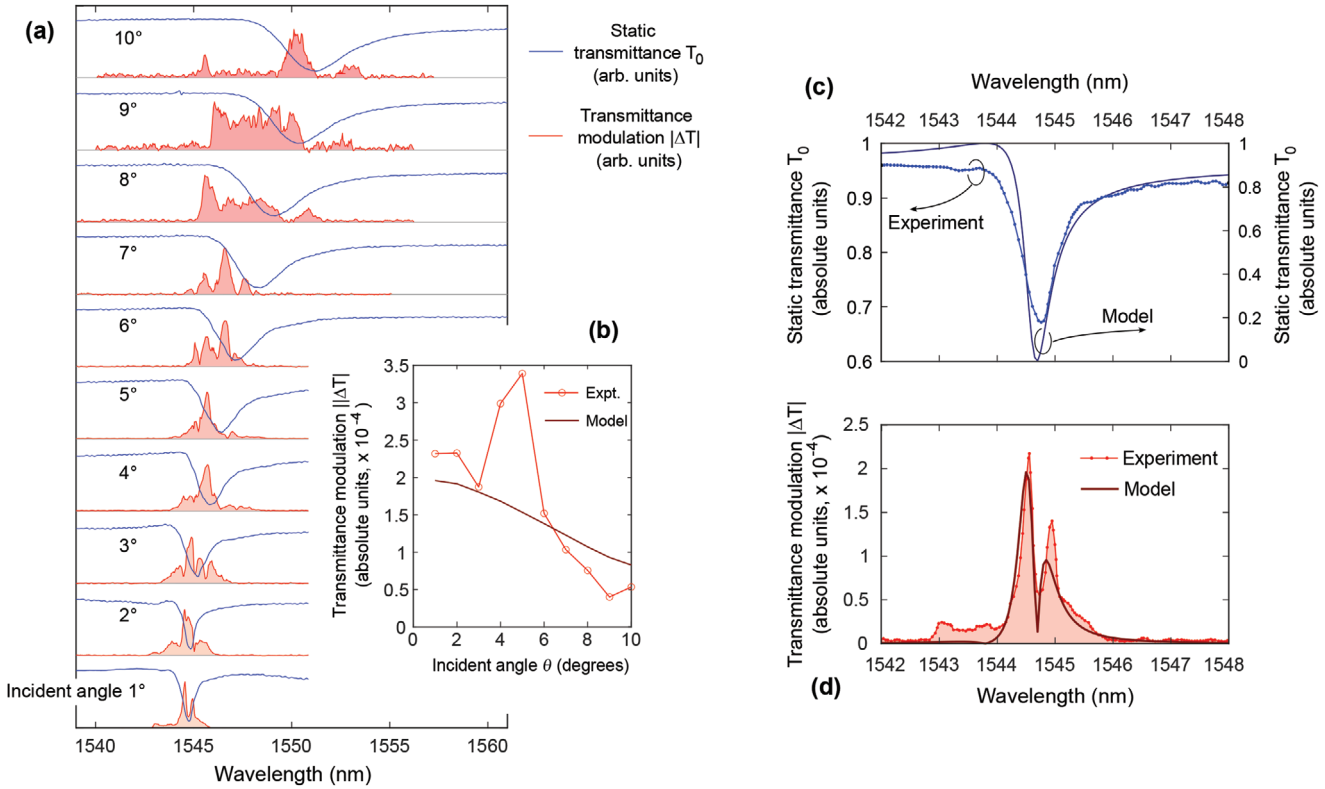

Figure 3. Angular and spectral properties of the metasurface modulation. a) Angle-dependent transmittance modulation spectra, compared with static transmittance spectra, indicate that modulation occurs in the vicinity of the angularly dispersive resonance. b) Angular trend of the transmittance modulation spectral maximum. c,d) Zoomed view of static and modulated transmittance spectra at 1° incidence angle.

measure the phase Φ_{Re}; this can, however, be accessed by using a measurement scheme employing a vector network analyzer.

2.2. Angular Dispersion of Modulation

In the first part of our experimental study, we analyzed the angle-dependent modulation effect at fixed modulation frequency. In detail, we employed a metasurface-IDT pair where the IDT (and, consequently, the RF source) was matched to $\Omega/2\pi = 1102.7$ MHz. The beam of a tunable laser with wavelength spanning over the telecom C-band was shone on the metasurface, and the static transmittance $T_0(\lambda)$ (i.e., that with RF off) was collected. Switching on the RF signal with a power of –21 dBm and sweeping the laser wavelength, we collected the modulation spectrum $|\Delta T(\lambda)|$. **Figure 3a** illustrates the static and dynamic spectral behavior of the nonlocal resonance under analysis. Here, T_0 very well matches the Fano lineshape function, with central wavelength and linewidth drifting with the incident angle (see also Figure 2; Section SIII, Supporting Information). The dynamic response, i.e., the transmittance modulation amplitude $|\Delta T(\lambda)|$, is reported as red curves, offset in order to be compared with the respective $T_0(\lambda)$. It can be noticed that the $|\Delta T|$ vanishes except for the wavelength range that surrounds the Fano dip of T_0; the width of such range increases with θ according to the decrease of the static transmittance Q-factor. While the spectra in Figure 3a are each normalized to its maximum in order to improve the clarity of the representation, in Figure 3b we report modulation data expressed in absolute units. Here, we plot, as a function of θ, the calculated and the measured maximum of each spectrum $|\Delta T(\lambda)|$. Consistently with the decreasing trend of resonance Q-factor for increasing angles (see Figure 2b), the theoretical transmittance modulation decreases monotonically with θ. In the experiment we observed an overall decreasing trend of the modulation $|\Delta T|$, with some deviation occurring however at $\theta = 4°$ and 5°. We attribute this observation to the error induced by the re-alignment procedure ($x - y$ sample position) after an angular rotation, in conjunction with a certain degree of spatial inhomogeneity (see later). Besides this mismatch, we found an excellent agreement in the order of magnitude of the modulation amplitude. In our coupling model we indeed have only a single fitting parameter, that is, the mechanical displacement δ_M; the curves in Figure 3b,d have been obtained using $\delta_M = 0.37$ pm, to be compared with $\delta_M \approx 0.28$ pm deduced independently via a procedure detailed in Section SX (Supporting Information).

In a further analysis, we have focused on the spectral lineshape of the static and dynamic transmittance observed for $\theta = 1°$. In Figure 3c,d we show, respectively, the spectra of T_0 and $|\Delta T|$, in absolute units, following from experiment and model. Both experimental spectra match very well the theoretical counterparts except for minor discrepancies. In the spectra of T_0, the experimental peak has indeed a minimum value of ≈0.67 as opposed to the value of 0 observed in the theory; this effect is attributed to scattering losses induced by imperfections in the metasurface

periodicity and hole shape, as well as to the finite beam width (Section SIII, Supporting Information). Concerning the modulation $|\Delta T(\lambda)|$, it can be noticed that in both experiment and model the spectral feature is a curve with two peaks separated by a dip, eventually originating from the wavelength derivative of $T_0(\lambda)$ (Equation 9). Due to the smallness of both real and imaginary parts of $(\omega_k - \omega_{k,0})/\omega_{k,0}$, that amount to $\approx 2 \cdot 10^{-8}$, the central wavelength and the linewidth of $|\Delta T(\lambda)|$ are the same as those of $T_0(\lambda)$. For the same reason, the time-averaged transmittance is not visibly affected by the presence/absence of the acoustic excitation. Considering the modulation spectra for larger values of the incident angle (Figure 3a), some deviations from the double-peak spectral shape are however observed. We attribute this phenomenon to two effects. First, the effective increment of the spot size occurring for larger incident angles leads to effectively probing of a larger area of the metasurface. Indeed, as follows from the analysis of a spatial mapping of the modulation (see Section SIX, Supporting Information), the metasurface response is not homogeneous, featuring instead fabrication-induced disorder that may be contributing to the aforementioned effect. Second, the contribution of higher order scattering mechanisms could be relevant. Indeed, it is known that even a small amount of roughness enables the population of optical modes at the same laser frequency but at $\boldsymbol{k}$'s different from that of the directly excited mode.[58] At the operating frequencies several optical modes exist (see Section SIII, Supporting Information), and in particular at larger θ we found a region rich of other modes, which could lead to a more efficient inter-modal scattering mechanism. The modulated, re-scattered optical energy could be eventually re-coupled to the free space and experimentally detected via the main optical mode, also without perfect resonance matching.

2.3. Frequency Response of Modulation and Modal Couplings

In the second part of our experimental study, we focused on the frequency response of the modulation, in order to gain insight over the bandwidth capabilities of our system, and to obtain a broader picture about the optomechanical coupling mechanisms behind the reported nonlocal metasurface modulation. To this aim we fixed the incident angle to $\theta = 1°$, since smaller angles would have led to light backscattering into the laser with consequent instabilities. As a preliminary characterization, we measured with a vector network analyzer the RF scattering parameter S_{11}, whose dips indicate the excitation of a SAW emitted from the IDTs (**Figure** 4a). Subsequently, we excited each IDT with the RF source with a sinusoidal signal at the appropriate Ω, measuring by means of the RF spectrum analyzer the optical transmittance modulation. Specifically, we determined $\overline{\Delta T_M} \equiv \langle \max_\lambda |\Delta T(\lambda)| \rangle$, where $\langle \cdot \rangle$ indicates the spatial averaging over the area of the metasurface facing the active IDT. The measured $\overline{\Delta T_M}$ are plotted in Figure 4b. Here, it can be noticed that an optomechanical response is observed for all the driving frequencies, with a clear monotonically increasing trend. The presence of a finite $\overline{\Delta T_M}$ for each of the investigated Ω's means that there is a nonzero coupling between the optical mode and some mechanical mode at the specific Ω. The exact determination of which mechanical mode is involved is not straightforward, for two reasons. First, as recently reported,[59] the mechanical wave undergoes strong scattering processes while crossing the interface between the exterior and the interior of the metamaterial. As a result, the whole set of Bloch modes at Ω are populated (isofrequency set, see Section SVII, Supporting Information), leading to a mechanical displacement that does not originate from a pure Bloch modal function $\boldsymbol{u}_{K,N}$. Second, fabrication-induced disorder can lead to a deviation from the Bloch mode picture, as disorder is known to promote the formation of states in the bandgaps (Urbach tails).[60] Since an ab-initio treatment of those two effects is presently unfeasible, we will interpret the data in Figure 4b semi-quantitatively, relying on the mechanical band structure of the perfectly periodic metasurface illustrated in Figure 4c,d. The former is a zoomed version of the latter, as indicated by the gray rectangle in Figure 4d. In both Figure 4c,d, the Bloch modes are colored according to their optomechanical coupling $g_{R\ell}^{(0)}$, see the color scale above Figure 4d. Bloch modes are also labeled by numbers, whose sequence follows from the order of modes at the Γ point. We will use the same numbering also to label modes far from the zone center, for those branches that can be followed and unambiguously identified. Notice that in the spectral region of the fabricated IDTs (960–1120 MHz) only mode 7 extends to the Γ point, with a minimum at $\Omega/2\pi = 1075$ MHz; its wavefunction at the Γ point was depicted in Figure 1d. Outside from Γ, other modes exist in the 960–1120 MHz region, with $g_{R\ell}^{(0)}$ spanning several orders of magnitude. Modes 2 and 7, as well as the Γ-X' branch of mode 6, have a mid-range $g_{R\ell}^{(0)} \approx 5 \cdot 10^{-5}$, while mode 3 features a large coupling value of $g_{R\ell}^{(0)} \approx 6 \cdot 10^{-4}$.

Let us first analyze the origin of a finite $\overline{\Delta T_M}$ for $\Omega/2\pi < 1075$ MHz, recalling that $\overline{\Delta T_M} \propto \Delta T \propto g_{R\ell} = f_K \cdot g_{R\ell}^{(0)}$. Two main mechanisms can be responsible for this phenomenon: first, it can originate from tail states of mode 7, i.e., eigenmodes occurring below the band minimum due to disorder effects. The existence of finite displacement close to the Γ point for $\Omega/2\pi < 1075$ MHz is confirmed by displacement interferometry, as discussed in Section SVII (Supporting Information). Moreover, a contribution from mode 3—which we know to be populated, see again Section SVII (Supporting Information)—could also occur. However, this requires that f_K has a non-negligible value for $|\boldsymbol{K}| \approx 1.5 \div 1.8\ \mu\text{m}^{-1}$, that are the typical momentum values of mode 3 in the selected frequency range (see Figure 4c,e). Within the most immediate hypothesis that the effectively coupled region had a size equal to the laser beam spot, i.e., 30 μm, one would have $f_K < 10^{-5}$ (Figure 4e), meaning that $g_{R\ell}$ would be suppressed with respect to $g_{R\ell}^{(0)}$ by at least five orders of magnitude. The situation would be even worse if the total metasurface size (150 μm) was employed. Nonetheless, a contribution to the modulation from mode 3 can appreciably occur if the effectively coupled region has a size of the order of 3 μm, which means $f_K \approx (0.5 \div 1) \cdot 10^{-1}$ in the $|\boldsymbol{K}| \approx 1.5 \div 1.8\ \mu\text{m}^{-1}$ range, and hence, considering the $g_{R\ell}^{(0)}$ values and Equation (9), a modulation level consistent with the experiment. We believe that such a small effectively coupled region size is reasonable, as it may originate from the effect of spatial inhomogeneities, that limits optomechanical coherency length and prevents it from extending out of micro-metric sized "islands" (see also Section SIX, Supporting Information). Interestingly, the finite coupling region approach justifies also the observed

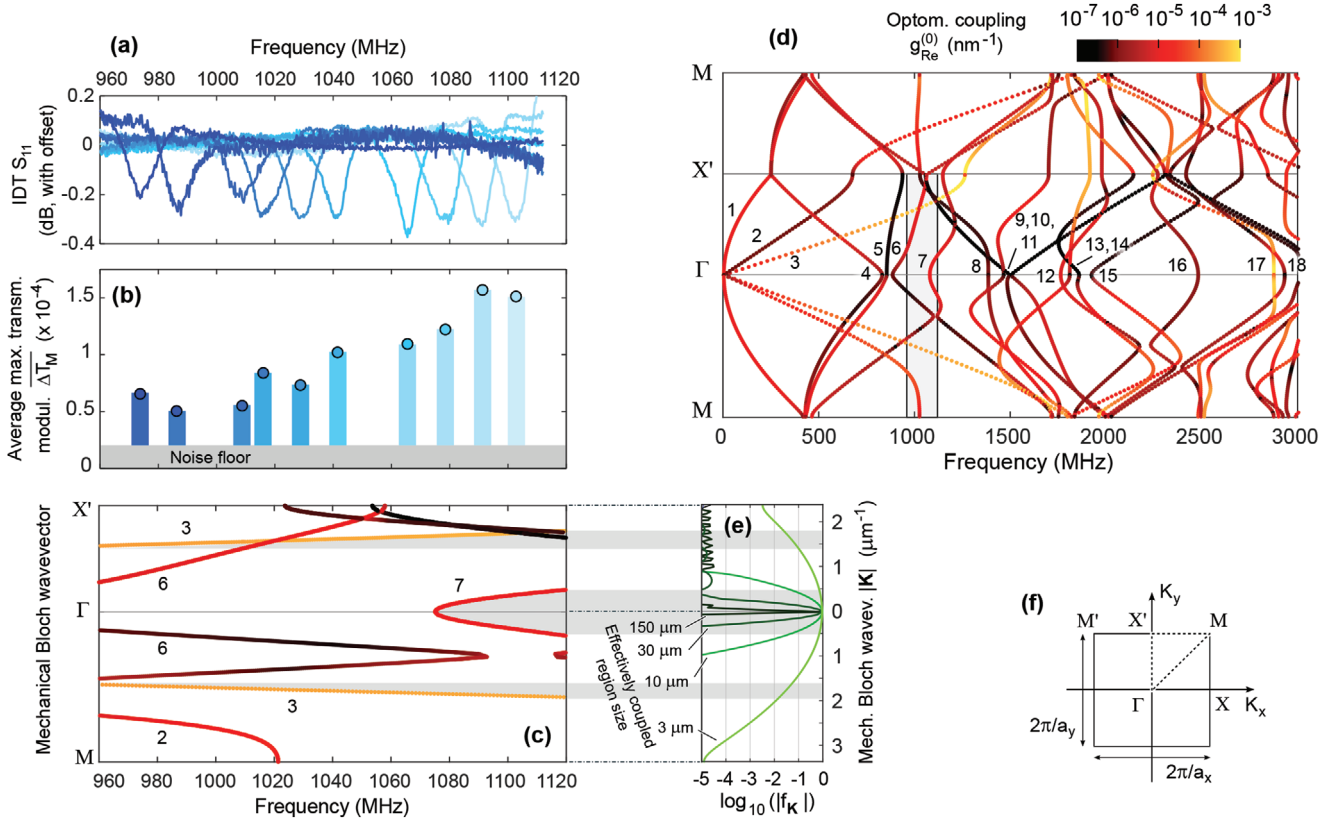

Figure 4. Frequency response of modulation and relation with mechanical band structure. a) RF reflection spectrum of interdigitated transducers (IDTs) with different center frequencies integrated in the chip. b), average maximum transmittance modulation (see text for the definition) collected from the metasurfaces coupled to the IDTs. The metasurfaces are nominally identical, only IDTs have different pitches. c,d) Calculated mechanical band structure and optomechanical coupling $g_{Re}^{(0)}$ (see Equation 2). Modes at Γ are labeled with increasing numbers. This numbering scheme is used to identify, when no ambiguity occurs, also modes far from Γ. Panel (c) is a zoomed version of the grey region in (d). e) Coupling factor f_K (see Equation 2) as a function of effectively coupled region size and of mechanical Bloch wavevector modulus. f) Representation of the Brillouin zone for the slightly rectangular crystal constituting the metasurface.

ΔT above 1075 MHz. Indeed, the ≈ 3 μm coupling region implies that f_K is a smooth function, and of order unity, in the $|K| < 0.5$ μm^{-1} interval. Since this interval is relevant for mode 7 (see Figure 4c,e), the mentioned behavior of f_K eventually allows for significant optomechanical coupling with all frequencies in the 1075–1105 MHz range. In particular, the increasing trend of $\overline{\Delta T_M}$ suggests that coupling with mode 7 is present in addition with coupling with mode 3. Indeed, spanning from 960 and 1120 MHz, mode 3 has a rather constant value of $g_{Re}^{(0)}$, while its $|K|$ is increasing: if the optomechanical effect originated only from mode 3, its strength would have decreased with increasing frequency due to the f_K trend.

2.4. Role of Symmetries on the Modulation Strength

The final part of our study is an analysis on the role of mirror plane symmetries on the optomechanical effect. As well known in solid-state physics, symmetries imply selection rules that eventually dictate allowed and forbidden processes involving multiple states. In our case, symmetries pose strong constraints on the finiteness of the coupling integrals $\Delta_{Re(Im)}$ and eventually of the coupling constants $g_{Re(Im)}$ and experimentally measurable modulation ΔT. The first observation is that, for zero slant angle β, our unit cell is invariant for the mirror symmetry operations $\hat{\sigma}_x$, $\hat{\sigma}_y$ and $\hat{\sigma}_z$, while for a finite β only $\hat{\sigma}_x$ and $\hat{\sigma}_y$ remain symmetries of the system. Since, however, in our sample β is small, we can start studying the structure with $\beta = 0$ and classify the mechanical eigenmodes and their couplings $g_{Re(Im)}^{(0)}$ according to the mode eigenvalues with respect to the operators $\hat{\sigma}_{x,y,z}$. Following the analysis outlined in Section SV (Supporting Information), it turns out that, for $\boldsymbol{K} = (0, 0)$ and $\boldsymbol{k} = (0, 0)$, the integral in Equation (6) can be written as

$$\Delta_{\mathrm{MB},Re} = -\frac{(1+\sigma_x)(1+\sigma_y)(1+\sigma_z)}{2D_{1/8}\,\delta_{\mathrm{ref}}} \int_{\partial D_{1/8}} \mathrm{d}S\, \Re(\boldsymbol{n}\cdot\boldsymbol{u}) \left(\Delta\varepsilon\, \boldsymbol{E}_{\parallel}\cdot\boldsymbol{E}_{\parallel} - \Delta\eta\, \boldsymbol{D}_{\perp}\cdot\boldsymbol{D}_{\perp}\right) \tag{10}$$

where $\sigma_{x,\,y,\,z}$ are the eigenvalues of the operators $\hat{\sigma}_{x,y,z}$ for the mechanical wavefunction $\boldsymbol{u}$, and the integral is taken over one appropriately chosen eighth of the unit cell. Analogous formulas hold

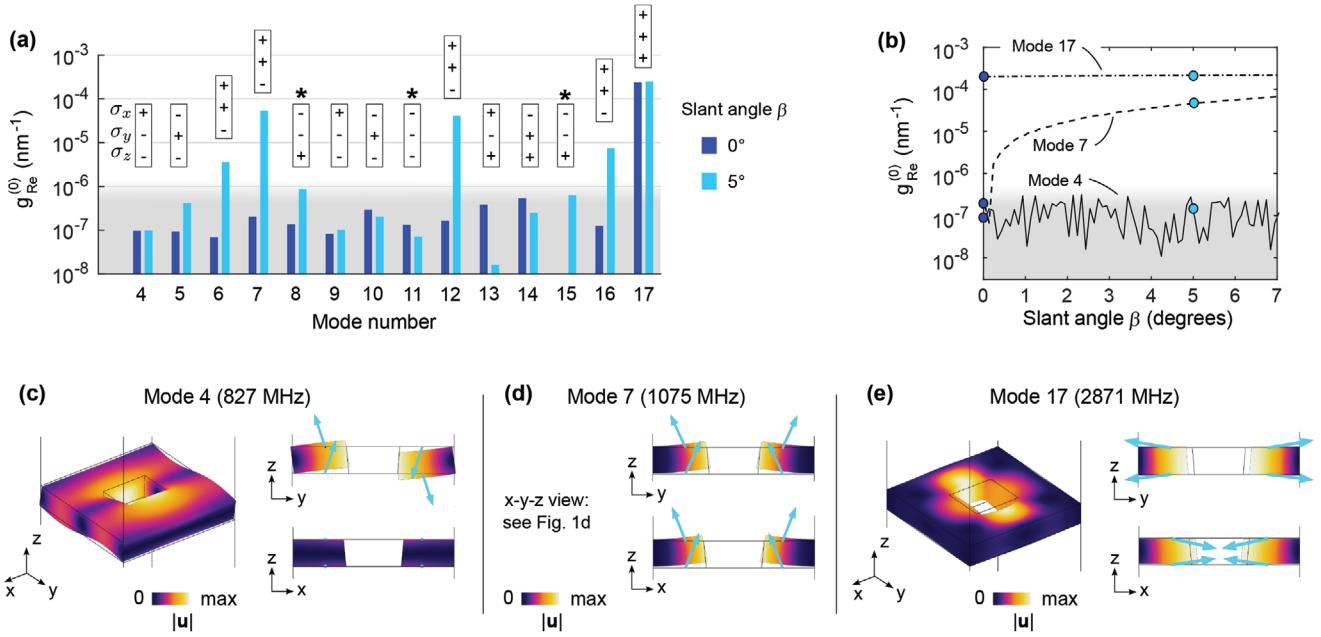

Figure 5. Symmetry analysis of optomechanical coupling. a) Optomechanical coupling for a set of mechanical modes (see Figure 4d for the numbering), calculated for two values of the hole slant angle (see Figure 1c). In the case $\beta = 0°$, finite coupling occurs if all among $\sigma_{x,\,y,\,z}$ equal +1. In the case $\beta = 5°$, finite coupling occurs if both σ_x and σ_y equal +1. Bars extending only in the gray region are numerical zeros. The modes marked with an asterisk require in principle two-mode (degenerate) perturbation theory, thus the results may be inaccurate. b) Dependence of the optomechanical coupling upon the symmetry-breaking parameter β, for modes with different symmetries. Mode 4 never couples because it has $\sigma_y = -1$. Mode 7 couples only for $\beta \neq 0°$ because it has both σ_x and σ_y equal to +1 but σ_z equal to –1. Mode 17 always couples, independently of β, because it has all $\sigma_{x,\,y,\,z}$ equal to +1. The gray region represents numerical zeros. Panels (c–e) represent the mechanical Bloch mode profile for the three modes analyzed in (b).

for $\Delta_{\mathrm{MB},\,Im}$ and $\Delta_{\mathrm{PE},\,Re(Im)}$. An immediate consequence of Equation (10) is that it is sufficient that only one among $\sigma_{x,\,y,\,z}$ equals –1 in order to have $\Delta_{Re} = \Delta_{Im} = 0$ (recall that the eigenvalues of mirror symmetry operators can only take ±1 values). Interestingly, the eigenvalue of the mirror symmetry operation for the e.m. wavefunction does not play any role since the integral is quadratic in the e.m. fields.

The predictive power of Equation (10) can be appreciated looking at **Figure 5a**, where we plot the values of $g_{Re}^{(0)}$ as blue bars for various mechanical modes at $\boldsymbol{K} = (0, 0)$ of the $\beta = 0°$ structure. Also the photonic $\boldsymbol{k}$ is chosen to be zero. Mechanical modes 1–3 are not considered here since they have zero frequency at the Γ point, leading to numerical instabilities. From Figure 5a it is evident that only mode number 17 has a finite coupling, i.e., a level of $g_{Re}^{(0)}$ that emerges out of the grey region, which represents a numerical zero background (originating from tiny asymmetries in the FEM solver mesh). Notably, mode 17 is the first mode without –1 among the symmetry eigenvalues (refer to Figure 4d for the numbering of eigenmodes), thus confirming the validity of Equation (10). When the condition $\beta = 0°$ is relaxed, Equation (10) would be replaced by its analogous without the $(1 + \sigma_z)$ factor and with the integral performed over one fourth of the unit cell. Thus, the condition to have finite coupling only requires that σ_x and σ_y both equal +1. In this framework, in addition to mode 17, also modes 6, 7, 12, and 16 should have $g_{Re} \neq 0$: this is exactly what resulted from numerical calculations for $\beta = 5°$ (Figure 5a, cyan bars). We also performed a fine sweep over β, obtaining the trends for $g_{Re}^{(0)}$ reported in Figure 5b. Here, one can notice that: (i) mode 4 has a coupling that always remains in the numerical zero region, (ii) mode 7 rapidly acquires a finite value upon increasing β, (iii) mode 17 has a coupling almost independent of β. This confirms the crucial role of symmetry eigenvalues of the mechanical modes in the determination of the optomechanical coupling. Moreover, it turns out that a very small deviation from full symmetry, i.e., a very small value of hole slant angle β, can be responsible for a significant value of the coupling constant, also for modes that would have zero coupling otherwise. To complete our picture, we plotted in Figure 5c–e visual representations of the displacement field $\Re(\boldsymbol{u})$ for the three modes analyzed above. Notice that these fields are calculated for the $\beta = 5°$ structure, thus in principle they do not have a definite character upon the σ_z operation. However, at least visually, a definite character stands out, and such character is exactly that of the σ_z eigenvalue determined for the mode of the $\beta = 0°$ structure. This supports once more the suitability of symmetry analysis for the study of coupling in slightly perturbed optomechanical slabs. As a final note, we highlight that, according to the analysis detailed in Section SV.A (Supporting Information), the mechanical modes with $\sigma_x = \sigma_y = -1$ (modes 8, 11, and 15) cannot be treated with the single-mode perturbation theory, as they couple the two quasi-degenerate photonic modes falling in our wavelength range. The bars reported in Figure 5a corresponding to those mechanical modes only take into account the diagonal perturbation elements; thus, the reported $g_{Re}^{(0)}$ values for those modes are subject to corrections. The analysis of this kind of optomechanical degenerate coupling in dispersive metasurfaces is likely a research topic of

interest for future studies, possibly leading to useful effects related, for instance, to polarization manipulation.

3. Discussion and Conclusion

In this work we have shown that, relying on a monolithic piezoelectric dielectric metasurface chip, nonlocal photonic resonances can be electrically modulated at gigahertz frequency. Experiments agree with numerical modeling and with symmetry analysis; similarly to recent reports about chirality,[61] the tuning of the metasurface holes slant angle appears as a precious tool for metasurface functionality control. In our samples, deviations from perfect periodicity induce spurious scattering, likely responsible for non-ideal modulation lineshapes; however, such nonidealities allow for a more broadband response with respect to what expected for a perfectly periodic metasurface. The present implementation also displays a rather small modulation amplitude; in this regards, future device generations could take advantage of various improvements that will easily raise the modulation by orders of magnitude. Indeed, SAW displacements in the order of 20˜nm are within current technological reach,[62] which would rescale the modulation into the 10^{-2} range according with Equation (9); further improvement could be achieved by integrating thin films of ZnO on the GaAs surface.[63] Although a modulation close to 100% is perhaps hardly achievable without radical platform innovations, it should be recalled that small amplitudes are commonly employed as modulation tones.[64,65] Future work on the modulation frequency response is another important front for future investigation. In our device, the modulation is limited in bandwidth to about 10 MHz around the interdigital transducer resonance, leading to a distorted impulse response in the time domain; such limitation can be overcome for instance by employing advanced transducer designs.[66] Finer lithographic processes would also allow for narrower transducer pitches, with multi-GHz frequencies likely within reach.

While our experiments are performed in a purely classical regime, quantum emitters can be easily integrated in the proposed platform, leading to interesting perspectives for quantum optomechanics.[67–70] Improving the quality factor of the photonic resonance, for instance relying on bound states in the continuum,[71] could enable low-power optical modulators, enhanced sensing schemes[72] and electrophononics.[73] Other applications such as space-time photonics and nonreciprocal devices could benefit from the outcomes of our study[74,75]; in parallel, basic science effects such as quantum Hall effect for light[76] could possibly find a feasible implementation in our system.

Supporting Information

Supporting Information is available from the Wiley Online Library or from the author.

Acknowledgements

The authors acknowledge Chiara Massetti for her contributions in an early stage of this project, as well as for preparing part of Figure 1. Dr. Paulo V. Santos is acknowledged for the interferometric displacement measurements and for insightful discussions. Dr. Marco Cecchini is acknowledged for support with the VNA measurements. A.P. acknowledges funding from the Alexander von Humboldt Foundation Experienced Researcher Fellowship program.

Open access publishing facilitated by Universita degli Studi di Pisa, as part of the Wiley - CRUI-CARE agreement.

Conflict of Interest

The authors declare no conflict of interest.

Data Availability Statement

The data that support the findings of this study are available from the corresponding author upon reasonable request.

Keywords

dispersive metasurface, photonic crystal, radiofrequency modulation

Received: May 10, 2024
Revised: October 22, 2024
Published online:

[1] H.-T. Chen, A. J. Taylor, N. Yu, *Rep. Prog. Phys.* **2016**, *79*, 076401.
[2] J. Hu, S. Bandyopadhyay, Y.-H. Liu, L.-Y. Shao, *Front. Phys.* **2021**.
[3] S. So, J. Mun, J. Park, J. Rho, *Adv. Mater.* **2023**, *35*, 2206399.
[4] J. Kim, J. Seong, W. Kim, G.-Y. Lee, S. Kim, H. Kim, S.-W. Moon, D. K. Oh, Y. Yang, J. Park, J. Jang, Y. Kim, M. Jeong, C. Park, H. Choi, G. Jeon, K. Lee, D. H. Yoon, N. Park, B. Lee, H. Lee, J. Rho, *Nat. Mater.* **2023**, *22*, 474.
[5] A. Overvig, A. Alù, *Laser Photonics Rev.* **2022**, *16*, 2100633.
[6] K. Shastri, F. Monticone, *Nat. Photonics* **2023**, *17*, 36.
[7] H. Kwon, D. Sounas, A. Cordaro, A. Polman, A. Alù, *Phys. Rev. Lett.* **2018**, *121*, 173004.
[8] C. Guo, M. Xiao, M. Minkov, Y. Shi, S. Fan, *Optica* **2018**, *5*, 251.
[9] A. Ji, J.-H. Song, Q. Li, F. Xu, C.-T. Tsai, R. C. Tiberio, B. Cui, P. Lalanne, P. G. Kik, D. A. B. Miller, M. L. Brongersma, *Nat. Commun.* **2022**, *13*, 7848.
[10] T. He, T. Liu, S. Xiao, Z. Wei, Z. Wang, L. Zhou, X. Cheng, *Sci. Adv.* **2022**, *8*, 9.
[11] S. C. Malek, A. C. Overvig, A. Alù, N. Yu, *Light: Sci. Appl.* **2022**, *11*, 246.
[12] K. Shastri, O. Reshef, R. W. Boyd, J. S. Lundeen, F. Monticone, *Optica* **2022**, *9*, 738.
[13] D. A. B. Miller, *Science* **2023**, *379*, 41.
[14] S. M. Kamali, E. Arbabi, A. Arbabi, A. Faraon, *Nanophotonics* **2018**, *7*, 1041.
[15] Y. Hu, X. Wang, X. Luo, X. Ou, L. Li, Y. Chen, P. Yang, S. Wang, H. Duan, *Nanophotonics* **2020**, *9*, 3755.
[16] L. Huang, L. Xu, D. A. Powell, W. J. Padilla, A. E. Miroshnichenko, *Phys. Rep.* **2023**, *1008*, 1.
[17] H. Jiang, K. Sun, Y. Jia, Y. Cai, U. Levy, Z. Han, *Adv. Opt. Mater.* **2024**, *12*, 2303229.
[18] K. Bi, Q. Wang, J. Xu, L. Chen, C. Lan, M. Lei, *Adv. Opt. Mater.* **2021**, *9*, 2001474.
[19] J. Yang, S. Gurung, S. Bej, P. Ni, H. W. Howard Lee, *Rep. Prog. Phys.* **2022**, *85*, 036101.
[20] Z. Guanxing, Z. Liu, W. Deng, W. Zhu, *Journal of Optics* **2021**, *23*, 013001.

[21] C. Jung, G. Kim, M. Jeong, J. Jang, Z. Dong, T. Badloe, J. K. W. Yang, J. Rho, *Chem. Rev.* **2021**, *121*, 13013.
[22] D. Kang, H. Heo, Y. Yang, J. Seong, H. Kim, J. Kim, J. Rho, *Opto-Electron. Adv.* **2024**, *7*, 230216.
[23] I. A. Ajia, J.-Y. Ou, N. J. Dinsdale, H. J. Singh, T. Chen-Sverre, T. Liu, N. I. Zheludev, O. L. Muskens, *Nano Lett.* **2021**, *21*, 4563.
[24] K. O'Brien, N. D. Lanzillotti-Kimura, J. Rho, H. Suchowski, X. Yin, X. Zhang, *Nat. Commun.* **2014**, *5*, 4042.
[25] J.-Y. Ou, E. Plum, J. Zhang, N. I. Zheludev, *Nat. Nanotechnol.* **2013**, *8*, 252.
[26] Q. Zhang, E. Plum, J.-Y. Ou, H. Pi, J. Li, K. F. MacDonald, N. I. Zheludev, *Adv. Opt. Mater.* **2021**, *9*, 2001826.
[27] I.-C. Benea-Chelmus, S. Mason, M. L. Meretska, D. L. Elder, D. Kazakov, A. Shams-Ansari, L. R. Dalton, F. Capasso, *Nat. Commun.* **2022**, *13*, 3170.
[28] H. Kwon, T. Zheng, A. Faraon, *Nano Lett.* **2021**, *21*, 2817.
[29] H. Kwon, T. Zheng, A. Faraon, *Nat. Commun.* **2022**, *13*, 5811.
[30] S.-Q. Li, X. Xu, R. Maruthiyodan Veetil, V. Valuckas, R. Paniagua-Domínguez, A. I. Kuznetsov, *Science* **2019**, *364*, 1087.
[31] M. I. Hussein, M. J. Leamy, M. Ruzzene, *Appl. Mech. Rev.* **2014**, *66*, 040802.
[32] M. M. D. Lima, P. V. Santos, *Rep. Prog. Phys.* **2005**, *68*, 1639.
[33] N. Courjal, S. Benchabane, J. Dahdah, G. Ulliac, Y. Gruson, V. Laude, *Appl. Phys. Lett.* **2010**, *96*, 131103.
[34] S. Kim, V. Gopalan, *Appl. Phys. Lett.* **2001**, *78*, 3015.
[35] S. A. Tadesse, M. Li, *Nat. Commun.* **2014**, *5*, 5402.
[36] S. Zanotto, G. Mazzamuto, F. Riboli, G. Biasiol, G. C. La Rocca, A. Tredicucci, A. Pitanti, *Nanophotonics* **2019**, *8*, 2291.
[37] Q. Yang, S. Kruk, Y. Xu, Q. Wang, Y. K. Srivastava, K. Koshelev, I. Kravchenko, R. Singh, J. Han, Y. Kivshar, I. Shadrivov, *Adv. Funct. Mater.* **2020**, *30*, 1906851.
[38] S. Collin, *Rep. Prog. Phys.* **2014**, *77*, 126402.
[39] C. Baker, W. Hease, D.-T. Nguyen, A. Andronico, S. Ducci, G. Leo, I. Favero, *Opt. Express* **2014**, *22*, 14072.
[40] K. C. Balram, M. Davanço, J. Y. Lim, J. D. Song, K. Srinivasan, *Optica* **2014**, *1*, 414.
[41] M. Dong, G. Clark, A. J. Leenheer, M. Zimmermann, D. Dominguez, A. J. Menssen, D. Heim, G. Gilbert, D. Englund, M. Eichenfield, *Nat. Photonics* **2022**, *16*, 59.
[42] Z. Luo, A. Zhang, W. Huang, S. Shao, Y. Liu, T. Wu, Y. Zou, *IEEE J. Sel. Top. Quantum Electron.* **2023**.
[43] D. A. Fuhrmann, S. M. Thon, H. Kim, D. Bouwmeester, P. M. Petroff, A. Wixforth, H. J. Krenner, *Nat. Photonics* **2011**, *5*, 605.
[44] D. Wigger, K. Gawarecki, P. Machnikowski, *Adv. Quantum Technol.* **2021**, *4*, 2000128.
[45] D. D. Bühler, M. Weiß, A. Crespo-Poveda, E. D. Nysten, J. J. Finley, K. Müller, P. V. Santos, M. M. de Lima, H. J. Krenner, *Nat. Commun.* **2022**, *13*, 6998.
[46] W. Jiang, R. N. Patel, F. M. Mayor, T. P. McKenna, P. Arrangoiz-Arriola, C. J. Sarabalis, J. D. Witmer, R. Van Laer, A. H. Safavi-Naeini, *Optica* **2019**, *6*, 845.
[47] A. E. Hassanien, S. Link, Y. Yang, E. Chow, L. L. Goddard, S. Gong, *Photonics Res.* **2021**, *9*, 1182.
[48] E. Klopfer, S. Dagli, D. Barton, M. Lawrence, J. A. Dionne, *Nano Lett.* **2022**, *22*, 1703.
[49] I. Marinković, M. Drimmer, B. Hensen, S. Gröblacher, *Nano Lett.* **2021**, *21*, 529.
[50] H. Weigand, V. V. Vogler-Neuling, M. R. Escalé, D. Pohl, F. U. Richter, A. Karvounis, F. Timpu, R. Grange, *ACS Photonics* **2021**, *8*, 3004.
[51] A. Weiss, C. Frydendahl, J. Bar-David, R. Zektzer, E. Edrei, J. Engelberg, N. Mazurski, B. Desiatov, U. Levy, *ACS Photonics* **2022**, *9*, 605.
[52] Z. Yu, X. Sun, *Light: Sci. Appl.* **2020**, *9*, 1.
[53] A. G. Primo, N. C. Carvalho, C. M. Kersul, N. C. Frateschi, G. S. Wiederhecker, T. P. M. Alegre, *Phys. Rev. Lett.* **2020**, *125*, 233601.
[54] W. Yan, P. Lalanne, M. Qiu, *Phys. Rev. Lett.* **2020**, *125*, 013901.
[55] M. Zhao, K. Fang, *Opt. Express* **2019**, *27*, 10138.
[56] S. Liu, H. Tong, K. Fang, *Nat. Commun.* **2022**, *13*, 3187.
[57] S. Zanotto, in Fano Resonances in Optics and Microwaves (Eds.: E. Kamenetskii, A. Sadreev, A. Miroshnichenko), Springer Nature Switzerland **2018**, Ch. 23.
[58] E. C. Regan, Y. Igarashi, B. Zhen, I. Kaminer, C. W. Hsu, Y. Shen, J. D. Joannopoulos, M. Soljačić, *Sci. Adv.* **2016**, *2*, 11.
[59] S. Zanotto, G. Biasiol, P. V. Santos, A. Pitanti, *Nature Communications* **2022**, *13*, 5939.
[60] S. John, *Phys. Rev. Lett.* **1987**, *58*, 2486.
[61] Y. Chen, H. Deng, X. Sha, W. Chen, R. Wang, Y.-H. Chen, D. Wu, J. Chu, Y. S. Kivshar, S. Xiao, C.-W. Qiu, *Nature* **2023**, *613*, 474.
[62] J. Hellemann, F. Müller, M. Msall, P. V. Santos, S. Ludwig, *Phys. Rev. Appl.* **2022**, *17*, 044024.
[63] B. Dong, M. E. Zaghloul, *Nanoscale Adv.* **2019**, *1*, 3537.
[64] S. Grillanda, M. Carminati, F. Morichetti, P. Ciccarella, A. Annoni, G. Ferrari, M. Strain, M. Sorel, M. Sampietro, A. Melloni, *Optica* **2014**, *1*, 129.
[65] S. Wald, F. Diorico, O. Hosten, *Appl. Opt.* **2023**, *62*, 1.
[66] M. Weiß, A. L. Hörner, E. Zallo, P. Atkinson, A. Rastelli, O. G. Schmidt, A. Wixforth, H. J. Krenner, *Phys. Rev. Appl.* **2018**, *9*, 014004.
[67] W. J. M. Kort-Kamp, A. K. Azad, D. A. R. Dalvit, *Phys. Rev. Lett.* **2021**, *127*, 043603.
[68] K. C. Balram, M. I. Davanço, J. D. Song, K. Srinivasan, *Nat. Photonics* **2016**, *10*, 346.
[69] K. C. Balram, K. Srinivasan, *Adv. Quantum Technol.* **2022**, *5*, 2100095.
[70] R. Stockill, M. Forsch, G. Beaudoin, K. Pantzas, I. Sagnes, R. Braive, S. Gröblacher, *Phys. Rev. Lett.* **2019**, *123*, 163602.
[71] S. Zanotto, G. Conte, L. C. Bellieres, A. Griol, D. Navarro-Urrios, A. Tredicucci, A. Martínez, A. Pitanti, *Phys. Rev. Appl.* **2022**, *17*, 044033.
[72] R. Shnaiderman, G. Wissmeyer, O. Ülgen, Q. Mustafa, A. Chmyrov, V. Ntziachristos, *Nature* **2020**, *585*, 372.
[73] A. V. Akimov, C. L. Poyser, A. J. Kent, *Semicond. Sci. Technol.* **2017**, *32*, 053003.
[74] D. B. Sohn, S. Kim, G. Bahl, *Nat. Photonics* **2018**, *12*, 91.
[75] E. A. Kittlaus, W. M. Jones, P. T. Rakich, N. T. Otterstrom, R. E. Muller, M. Rais-Zadeh, *Nat. Photonics* **2021**, *15*, 43.
[76] K. Fang, Y. Wang, *Phys. Rev. Lett.* **2019**, *122*, 233904.